

Article

# Investigation of Thermal Behavior of Layered Double Hydroxides Intercalated with Carboxymethylcellulose Aiming Bio-Carbon Based Nanocomposites

Vagner R. Magri <sup>1</sup>, Alfredo Duarte <sup>1</sup>, Gustavo F. Perotti <sup>1,2</sup> and Vera R.L. Constantino <sup>1,\*</sup>

<sup>1</sup> Departamento de Química Fundamental, Instituto de Química, Universidade de São Paulo (USP), Av. Prof. Lineu Prestes 748, São Paulo CEP 05508-000, SP, Brazil; vrmagri@usp.br (V.R.M.); aduarte@iq.usp.br (A.D.); gustavoperotti@ufam.edu.br (G.F.P.)

<sup>2</sup> Instituto de Ciências Exatas e Tecnologia, Universidade Federal do Amazonas (UFAM), Rua Nossa Senhora do Rosário 3863, Itacoatiara CEP 69103-128, AM, Brazil

\* Correspondence: vrlconst@iq.usp.br; Tel.: +55-11-3091-9152

Received: 31 March 2019; Accepted: 27 May 2019; Published: 1 June 2019



**Abstract:** Carboxymethylcellulose (CMC), a polymer derived from biomass, was intercalated into layered double hydroxides (LDH) composed by  $M^{2+}/Al^{3+}$  ( $M_2Al$ -CMC,  $M = Mg$  or  $Zn$ ) and evaluated as precursors for the preparation of biocarbon-based nanocomposites by pyrolysis.  $M_2Al$ -CMC hybrids were obtained by coprecipitation and characterized by X ray diffraction (XRD), vibrational spectroscopies, chemical analysis, and thermal analysis coupled to mass spectrometry. Following, pyrolyzed materials obtained between 500–1000 °C were characterized by XRD, Raman spectroscopy, scanning electron microscopy (SEM) and energy dispersive spectroscopy (EDS). Above 600 °C, Raman spectra of all samples showed the presence of graphitic carbon, which plays a role in the degree of crystallinity of produced inorganic phases (for comparison purposes,  $M_2Al$ - $CO_3$  materials were investigated after calcination in the same experimental conditions). XRD patterns of  $Mg_2Al$ -CMC pyrolyzed between 600–1000 °C showed poorly crystallized MgO and absence of spinel reflections, whereas for  $Zn_2Al$ -CMC, it was observed well crystallized nanometric ZnO at 800 °C, and  $ZnAl_2O_4$  and  $\gamma$ - $Al_2O_3$  phases at 1000 °C. Above 800 °C, the carbothermic reaction was noticed, transforming ZnO to zinc vapour. This study opens perspectives for nanocomposites preparation based on carbon and inorganic (mixed) oxides through precursors having organic-inorganic interactions at the nanoscale domain.

**Keywords:** intercalation compounds; layered materials; layered double hydroxides; hydrotalcite; thermal analysis; carboxymethylcellulose; carbon-based nanocomposites

## 1. Introduction

More than forty minerals have been identified as layered double hydroxide (LDH) phases which structures are analogous to brucite mineral,  $Mg(OH)_2$  [1]. In nature, partial replacement of magnesium ions by  $Al^{3+}$ ,  $Fe^{3+}$ ,  $Cr^{3+}$ ,  $Mn^{3+}$  or  $Co^{3+}$  produces an excess of positive charges in the structure that are neutralized by simple counter ions such as carbonate, hydroxide, sulphate or chloride. In some minerals, divalent cations like  $Zn^{2+}$ ,  $Ni^{2+}$ ,  $Fe^{2+}$  or  $Mn^{2+}$  are present instead of magnesium. These materials are also called as hydrotalcite-type compounds given that the first identified LDH phase was nominated hydrotalcite (due to its textural resemblance with talc) [2].

The chemical composition of LDH materials is usually represented by the general formula  $[(M^{2+}_{(1-x)}M^{3+}_x)(OH)_2]^{x+}[A^{m-}_{x/m}\cdot nH_2O]^{x-}$  and denoted as  $M^{2+}_R M^{3+}_A$ , where  $M$  is the metal ion,  $R$  is the  $M^{2+}/M^{3+}$  molar ratio and  $A^{m-}$  is a hydrated anion [2,3]. The  $M^{2+}/M^{3+}$  molar ratio in the minerals is usually 3 or 2 as for example in hydrotalcite ( $[Mg_6Al_2(OH)_{16}]CO_3\cdot 4H_2O$ ) and quintinite

( $[\text{Mg}_4\text{Al}_2(\text{OH})_{12}]\text{CO}_3 \cdot 3\text{H}_2\text{O}$ ), respectively [1]. In LDH structure, hydroxide ions are in a hexagonal close-packed arrangement in two adjacent planes in such a way that octahedral sites are occupied by metal cations (Figure 1a). The octahedra are edge-sharing along the crystallographic axes  $a$  and  $b$ , forming two-dimensional (2D) structures as shown in Figure 1b [3]. Positive layers are stacked along the  $c$ -axis and the anions are intercalated between them [3]. Different layers stacking of the same material can produce LDH structures with different dimensions along  $c$  direction, i.e., distinct polytypes: 3R (rhombohedral symmetry) or 2H (hexagonal symmetry) [3].

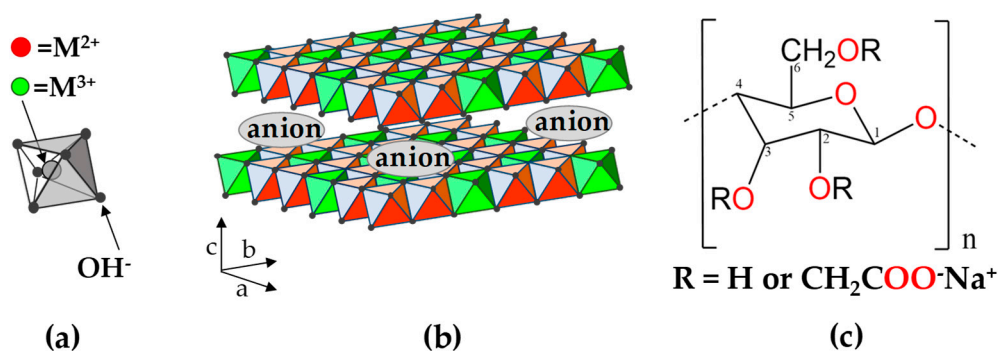


**Figure 1.** Schematic representation of (a) hydroxide ions coordinated to metal cation in an octahedral arrangement, (b) layered double hydroxide (LDH) structure comprising stacked positive layers intercalated by negative ions, (c) monomeric unit of carboxymethylcellulose (CMC).

From the 1970s, synthetic materials similar to LDH minerals have been prepared in a laboratory and characterized by increasingly advanced physicochemical techniques [4]. Such materials are very versatile in terms of the chemical composition of layers, as well as  $\text{M}^{2+}/\text{M}^{3+}$  molar ratio, and a great number of combinations with different anions can be employed in LDH synthesis. Instead of simple anions, LDH hybrid materials can be synthesized by the intercalation of polyoxometalates [5], anionic metal complexes [6] and organic species like drugs, dyes, amino acids, synthetic polymers and biopolymers [4,7,8]. Owing to their compositional versatility, a variety of LDH with different physical-chemical properties can be obtained for diverse applications, ranging from heterogeneous catalysis [9], environmental remediation [10], energy production [11], drug carrier and diagnosis in medicine [12] up to nanoreactors for prebiotic life [13].

LDH organic-inorganic hybrid materials have significant potential as precursors for nanocomposites based on mixed metal oxides (MMO) and carbonaceous species (C). Through calcination, LDH can be converted into oxides ( $\text{MO}_x$ ) and spinels ( $\text{M}_1\text{M}_2\text{O}_4$ ) which display  $\text{M}^{2+}-\text{O}^{2-}$  and  $\text{M}^{3+}-\text{O}^{2-}$  acid-basic sites, high specific surface area, well dispersed metals and fine tuning interface of components species suitable for adsorption and/or heterogeneous catalysis in a wide range of reactions [14–16]. Some studies have reported the preparation of MMO/C composites by the bottom-up method where an organic source is carbonized within the confined space between LDH layers [17]. This approach reduces the number of synthetic steps compared to the physical mixture of pre-prepared LDH and nanocarbon form (e.g., carbon nanotubes or graphene oxide), allowing isolation of porous carbon and yielding more homogeneous materials at submicroscale, fostering synergistic effects. Metal oxides (or hydroxides) and carbonaceous materials show exciting adsorption and catalytic properties suitable for applications in environmental remediation or development of sensors [17].

In this study, LDH materials composed by zinc, magnesium and aluminum cations intercalated with carboxymethylcellulose (CMC) polymer were chosen to investigate the thermal preparation of MMO/C composites. CMC is a water-soluble anionic polymer obtained through chemical modification of cellulose polysaccharide, the most abundant natural polymer [18]. Such polymer is constituted by a chain of glucose rings connected by  $\beta$ -1,4 glycosidic linkages between C(1) and C(4) of adjacent units, with a carboxymethyl-substituted group mainly at C(6) position (Figure 1c). As a biomass derivative,

CMC is a low-cost, abundant and sustainable source for biocarbon production and, as an anionic polyelectrolyte, can be intercalated into LDH structure. Small organic species intercalated into LDH can be volatilized even under pyrolytic conditions precluding the carbon formation. The usage of polymeric organic species increases the possibility of carbon production in a non-oxidizing atmosphere.

Few studies were reported about systems comprising LDH and CMC but none of them focused on the preparation of MMO/C nanocomposites.  $Mg_{1.15}Al$ -CMC material was prepared by exfoliation of nitrate-LDH in formamide and posterior restacking in a sodium CMC solution also in the organic solvent [19]. Later  $M_2Al$ -CMC ( $M = Mg, Zn, Cu, Ni$ ) materials were isolated by coprecipitation method [20,21].

In this work, composite materials based on MMO/C were prepared at four temperature values (500, 600, 800 and 1000 °C) through pyrolysis of  $M_2Al$ -LDH ( $M = Mg^{2+}$  or  $Zn^{2+}$ ) intercalated with CMC, as represented in Figure 2. LDH materials constituted by  $Mg^{2+}/Al^{3+}$  and  $Zn^{2+}/Al^{3+}$  were chosen owing to dissimilar characteristics as thermal stability [22] and topological transformation from LDH to MMO [23,24]. Otherwise, for comparison purposes, LDH materials containing intercalated carbonate instead of CMC were also prepared to investigate the probable influence of CMC on the inorganic phases achieved in the pyrolysis process. Nanocomposites comprising of graphitic carbon, metal oxides and spinel phases were produced within the 600–1000 °C range. For the LDH hybrid material containing  $Zn^{2+}$  ions, ZnO nanocrystals were observed when pyrolysis was performed at 800 °C; zinc oxide underwent a carbothermic reaction at higher temperatures. Whereas, XRD pattern of  $Mg_2Al$ -CMC exhibited only MgO phase within the 600–1000 °C range, indicating that pyrolyzed CMC hindered the spinel phase crystallization.

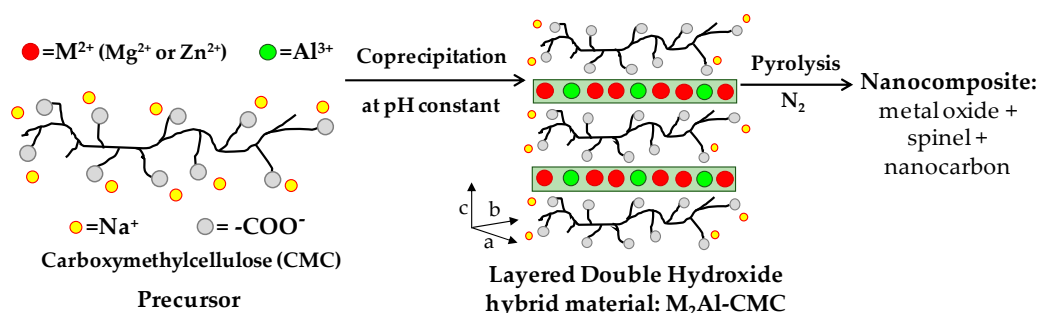


**Figure 2.** Schematic representation of the two-step synthetic approach used to produce MMO/carbon nanocomposites from layered double hydroxides.

## 2. Materials and Methods

### 2.1. Chemicals

Magnesium nitrate hexahydrate ( $Mg(NO_3)_2 \cdot 6H_2O$ , Merck), aluminum nitrate nonahydrate ( $Al(NO_3)_3 \cdot 9H_2O$ , Merck), zinc nitrate hexahydrate ( $Zn(NO_3)_2 \cdot 6H_2O$ , Merck), magnesium chloride hexahydrate ( $MgCl_2 \cdot 6H_2O$ , Sigma-Aldrich), aluminum chloride hexahydrate ( $AlCl_3 \cdot 6H_2O$ , Sigma-Aldrich), zinc chloride ( $ZnCl_2$ , Sigma-Aldrich), sodium hydroxide (NaOH, Sigma-Aldrich), sodium carbonate ( $Na_2CO_3$ , Merck), sodium carboxymethylcellulose—CMC (90 kDa, Degree of substitution 0.7, Sigma-Aldrich) were used without further purification. Deionized water was used in all experimental procedures.

### 2.2. Preparation of LDH-CMC Hybrid Materials

The intercalation of CMC polymer into LDH was carried out by co-precipitation method and the best experimental conditions are described ahead. For the preparation of the  $Mg_2Al$ -CMC sample, 3.070 g of CMC was solubilized into 250 mL of deionized water and the pH value of the solution was adjusted to 9.5 by the addition of NaOH 0.2 mol·L<sup>-1</sup> solution. Afterwards, 250 mL of an aqueous

solution containing 16.67 mmol of  $\text{MgCl}_2 \cdot 6\text{H}_2\text{O}$  and 8.83 mmol of  $\text{AlCl}_3 \cdot 6\text{H}_2\text{O}$  was added dropwise to CMC solution under a nitrogen atmosphere and vigorous stirring. The pH value was maintained constant by the addition of  $\text{NaOH}$   $0.2 \text{ mol} \cdot \text{L}^{-1}$  solution. The co-precipitation reaction was carried at  $60^\circ\text{C}$  and, after the complete addition of the metal cations solution, the suspension was maintained for 6 h at  $60^\circ\text{C}$ . The white precipitate was centrifuged, washed four times with deionized water and dried at room temperature under reduced pressure.

For the preparation of the  $\text{Zn}_2\text{Al}$ -CMC sample, 20 g of CMC was solubilized into 850 mL of deionized water and the pH value of the solution was adjusted to 7.5 by the addition of  $\text{NaOH}$   $0.5 \text{ mol} \cdot \text{L}^{-1}$  solution. Afterwards, 520 mL of an aqueous solution containing 41.20 mmol of  $\text{ZnCl}_2$  and 21.41 mmol of  $\text{AlCl}_3 \cdot 6\text{H}_2\text{O}$  was added dropwise to CMC solution under a nitrogen atmosphere, vigorous stirring and at room temperature. The pH value was maintained constant by the addition of  $\text{NaOH}$   $0.5 \text{ mol} \cdot \text{L}^{-1}$  solution. After addition of the metal cations solution, the suspension was dialyzed for 3 days changing the water after each 12 h. The white precipitate was then freeze dried.

For comparison purpose,  $\text{Mg}^{2+}/\text{Al}^{3+}$  and  $\text{Zn}^{2+}/\text{Al}^{3+}$  LDH materials intercalated with carbonate anion ( $\text{Mg}_2\text{Al-CO}_3$  and  $\text{Zn}_2\text{Al-CO}_3$ ) were synthesized as described by Miyata [25] with modifications. Typically, the pH value of 250 mL of water was adjusted to 9.5 (for  $\text{Mg}_2\text{Al-CO}_3$ ) or 9.0 (for  $\text{Zn}_2\text{Al-CO}_3$ ) by the addition of  $\text{Na}_2\text{CO}_3$   $0.2 \text{ mol} \cdot \text{L}^{-1}$  solution. To this solution, 250 mL of a solution containing 16.67 mmol of  $\text{Mg}(\text{NO}_3)_2 \cdot 6\text{H}_2\text{O}$  (or  $\text{Zn}(\text{NO}_3)_2 \cdot 6\text{H}_2\text{O}$ ) and 8.33 mmol of  $\text{AlCl}_3 \cdot 6\text{H}_2\text{O}$  was added dropwise under stirring. The co-precipitation reaction was carried out at an ambient atmosphere and room temperature. The pH value was maintained constant by the addition of  $\text{Na}_2\text{CO}_3$   $0.2 \text{ mol} \cdot \text{L}^{-1}$  solution. After addition of the metal cations solutions, the suspension was maintained under stirring at ambient atmosphere and room temperature for 2 h. The white precipitate was centrifuged, washed five times with deionized water, one time with ethanol and dried at room temperature under reduced pressure.

### 2.3. Preparation of MMO/C Composites

$\text{Mg}_2\text{Al}$ -CMC and  $\text{Zn}_2\text{Al}$ -CMC precursors were pyrolyzed on a Shimadzu TGA-50 furnace under a molecular nitrogen flow of  $50 \text{ mL min}^{-1}$ , using alumina crucibles and a heating rate of  $10^\circ\text{C min}^{-1}$ , at temperatures of 500, 600, 800 and  $1000^\circ\text{C}$ . For comparison purpose,  $\text{Mg}_2\text{Al-CO}_3$  and  $\text{Zn}_2\text{Al-CO}_3$  were calcined under nitrogen flow using the same parameters. Besides,  $\text{Mg}_2\text{Al}$ -CMC and  $\text{Zn}_2\text{Al}$ -CMC precursors were also calcined under synthetic air at  $1000^\circ\text{C}$ , using the same conditions described to pyrolysis at  $\text{N}_2$  environment. Afterwards, heated samples were stored in a desiccator containing silica gel under reduced pressure.

### 2.4. Physical Measurements

Elemental chemical analysis (carbon and hydrogen) were performed on a Perking Elmer model 2400 analyzer. Magnesium, zinc and aluminum contents were determined in triplicate by inductively coupled plasma optical emission spectroscopy (ICP OES) on a Spectro Arcos spectrometer. Both analyses were performed at the Central Analítica of Instituto de Química da Universidade de São Paulo (CA-IQUSP).

Mass spectrometry coupled to simultaneous thermogravimetric analysis and differential scanning calorimetry (TG-DSC-MS) were performed on a Netzsch thermoanalyzer model TGA/DSC 409 PC Luxx coupled to an Aëolos 403 C mass spectrometer under synthetic air or  $\text{N}_2$  flow of  $50 \text{ mL min}^{-1}$  employing alumina crucibles and a heating rate of  $10^\circ\text{C} \cdot \text{min}^{-1}$ .

X ray diffraction (XRD) patterns of powdered samples were recorded on a Bruker diffractometer model D8 DISCOVER equipped with Nickel-filtered  $\text{CuK}\alpha$  radiation ( $0.15418 \text{ nm}$ ), operating at 40 kV, 30 mA, sample rotating at 20 rpm, from  $1.5$  to  $70^\circ$  ( $2\theta$ ) at  $0.05^\circ$  intervals, 3 s per interval.

Fourier transform infrared (FTIR) spectra of powdered samples were recorded in the  $4000$ – $400 \text{ cm}^{-1}$  range on a Bruker Alpha spectrometer using a single bounce attenuated total diffuse reflectance (ATR) mode with a diamond crystal. Fourier transform Raman (FT-Raman) spectra were recorded on an FT-Raman Bruker FRS-100/S instrument using  $1064 \text{ nm}$  excitation radiation ( $\text{Nd}^{3+}/\text{YAG}$  laser) and liquid

nitrogen cooled Ge detector. Raman spectra of pyrolyzed samples were recorded in the 3500–100  $\text{cm}^{-1}$  range on a Renishaw inVia instrument coupled to a confocal Leica microscope and a CCD detector, using 532 nm excitation radiation ( $\text{Nd}^{3+}$ /YAG laser).

Scanning Electron (SEM) micrographs were collected using a JEOL JSM7401F instrument, equipped with a field emission gun (FEG). Accelerating voltages (kV) are reported on each micrograph. Energy Dispersive X ray Spectra (EDS) were collected simultaneously on a Thermo Fischer Scientific detector, Pioneer model, 30  $\text{mm}^2$  Si Crystal, coupled to a Noran System Six signal processor (NSS). Powder samples were pulverized onto carbon conductive tapes prior to SEM imaging.

### 3. Results and Discussion

#### 3.1. Characterization of LDH-CMC Hybrid Materials

XRD patterns of LDH- $\text{CO}_3$  and LDH-CMC synthesized samples showed profiles characteristic of layered double hydroxides (Figure 3). LDH- $\text{CO}_3$  samples are more crystalline than LDH-CMC, as evidenced by the high intensity and narrow diffraction peaks which can be indexed assuming a hexagonal cell with rhombohedral symmetry (3R polytype) and R-3m space group. The reflections observed at  $2\theta$  values below  $30^\circ$  are assigned to the (00l) planes that are related to interlayer distance ( $d_{\text{basal}}$ ) and the cell parameter  $c$  (Figure 1b). The reflection observed in  $2\theta$  values in the region of  $60^\circ$  is attributed to the (110) plane related to the cell parameter  $a$  that gives the average distance between metal cations in the layer. The presence of broad XRD peaks associated with both (003) and (110) planes of LDH-CMC samples indicates that the crystal dimensions are both reduced in the crystallographic directions  $a$  and  $c$  in comparison to LDH- $\text{CO}_3$  materials [26]. Table S1 (Supplementary Materials) shows the  $2\theta$  values, the respective interplane distances ( $d_{\text{hkl}}$ ) and the calculated unit cell parameters for LDH materials. For  $\text{Zn}_2\text{Al-CO}_3$  and  $\text{Mg}_2\text{Al-CO}_3$  samples, the  $d_{003}$  spacing values were respectively 0.754 nm and 0.765 nm. Samples  $\text{Zn}_2\text{Al-CMC}$  and  $\text{Mg}_2\text{Al-CMC}$  showed a shift of 003 diffraction peaks to 2.492 and 1.715 nm, respectively, indicating an expansion of the interlayer space in order to accommodate the macromolecules.

XRD pattern of  $\text{Mg}_2\text{Al-CMC}$  sample prepared by Yadollahi and Namazi [20] presented  $d_{003}$  spacing value equal to 1.73 nm while  $\text{Zn}_2\text{Al-CMC}$  sample reported by Yadollahi et al. [21] showed the  $d_{003}$  value of 1.58 nm. Considering that CMC is a polymer that may present different arrangements, the proposal of a conformation for the chains between the LDH layers is not straightforward. The basal spacing difference between  $\text{Mg}_2\text{Al-CMC}$  and  $\text{Zn}_2\text{Al-CMC}$  materials prepared in this work may be related to the higher water and CMC contents in the zinc matrix. The calculated  $d_{110}$  values for  $\text{Zn}_2\text{Al-CO}_3$  and  $\text{Zn}_2\text{Al-CMC}$  were 0.153 nm, while for  $\text{Mg}_2\text{Al-CO}_3$  and  $\text{Mg}_2\text{Al-CMC}$  were 0.152 nm and 0.151 nm, respectively, which means that the molar ratio between the metal cations is similar in the samples. These points will be discussed later when chemical elemental analysis will be presented.

XRD pattern of NaCMC exhibits mainly one broad peak around  $2\theta$  value of  $20^\circ$  (Figure S1, Supplementary Materials) which is associated with the low degree of organization of the macromolecules [27]. Considering the XRD patterns of LDH-CMC samples, it is observed a broad hump at ( $2\theta$ )  $20^\circ$  that could suggest that part of the polymer chains might not be confined within the interlayer space but rather adsorbed over LDH particles. XRD patterns of  $\text{M}_2\text{Al-CMC}$  ( $\text{M}^{2+} = \text{Mg}, \text{Zn}, \text{Ni}, \text{Cu}$ ) samples reported in the literature [21] also showed a broad peak in the same region.

The infrared and FT-Raman spectra of  $\text{Zn}_2\text{Al-CO}_3$  and  $\text{Mg}_2\text{Al-CO}_3$  are shown in Figure 4. The discussion about vibrational data is presented in Supplementary Materials, as well as a tentative attribution of the main vibrational bands (Table S2).

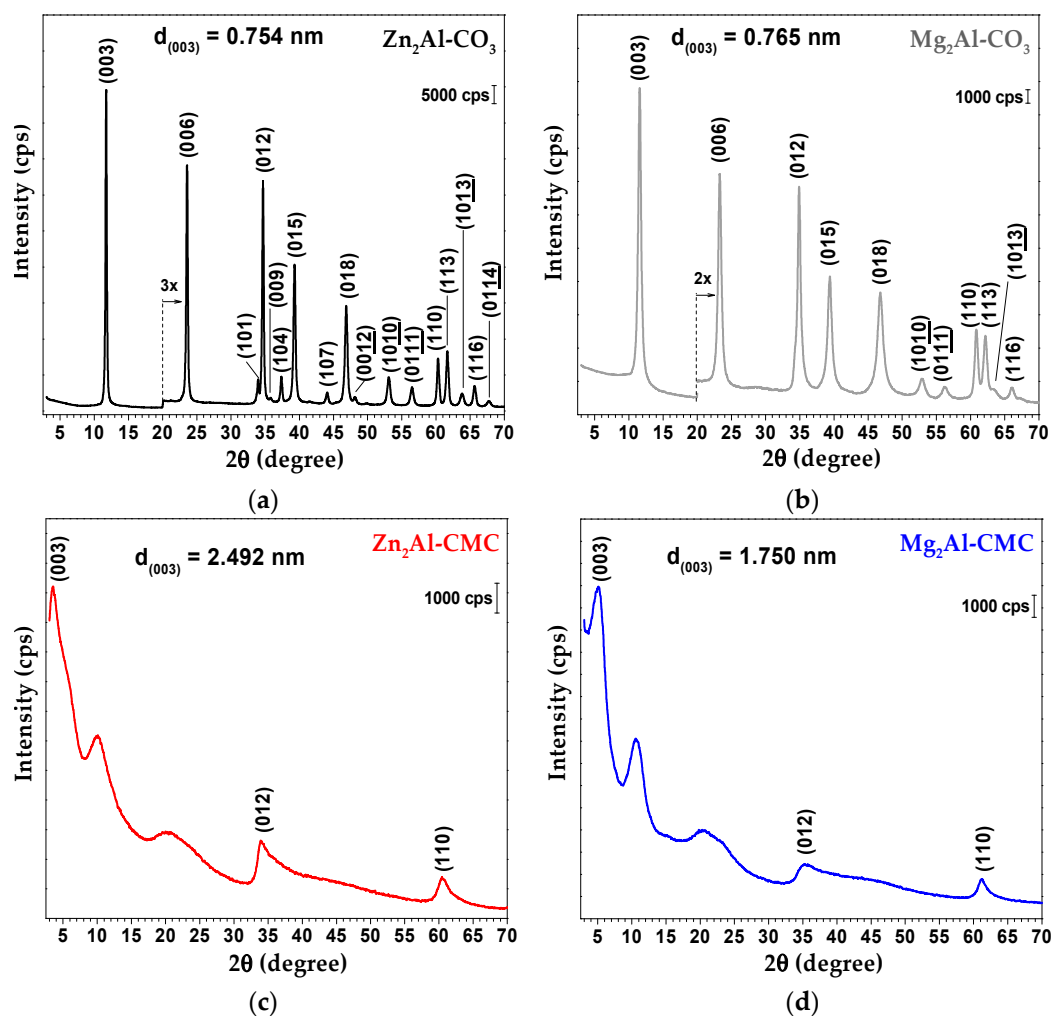


**Figure 3.** XRD patterns of  $\text{Zn}_2\text{Al-CO}_3$  (a),  $\text{Mg}_2\text{Al-CO}_3$  (b),  $\text{Zn}_2\text{Al-CMC}$  (c) and  $\text{Mg}_2\text{Al-CMC}$  (d) samples. The diffraction peaks in (a,b) were indexed according to ICSD 190041 and 86655, respectively.

The spectroscopic characterization of sodium CMC and LDH-CMC samples was evaluated by FTIR-ATR and FT-Raman spectroscopies (Figure 4). Spectra of the polymer and hybrid materials are very similar, and the results clearly indicate the presence of CMC in the LDH structure. A tentative attribution regarding cellulose and carboxymethylcellulose spectroscopic data is presented in Table 1. The NaCMC bands attributed to antisymmetric and symmetric stretching of carboxylate groups are noticed at  $1585\text{ cm}^{-1}$  ( $\nu_{as}\text{COO}^-$ ) and  $1412\text{ cm}^{-1}$  ( $\nu_s\text{COO}^-$ ), respectively. In the LDH-CMC spectra, the  $\nu_{as}\text{COO}^-$  band is shifted to  $1577\text{ cm}^{-1}$ . The  $\Delta\nu\text{COO}^-$  values calculated by the formula  $\Delta\nu\text{COO}^- = \nu_{as} - \nu_s$  are very close to that one of NaCMC, indicating an electrostatic interaction of carboxylate groups with LDH layers. Bands in the  $1100\text{--}980\text{ cm}^{-1}$  region are assigned to stretching and bending vibration of C–O bond from the glycosidic ring and hydroxyl groups. FT-Raman spectra of NaCMC and the hybrid materials show very similar bands. The band at  $2907\text{ cm}^{-1}$  is related to C–H stretching, at  $1118\text{ cm}^{-1}$  is attributed to symmetric stretching of C(1)–O–C(4) group and ring breathing, and at  $918\text{ cm}^{-1}$  is assigned to bending C(5)C(6)–H and HC(6)O.

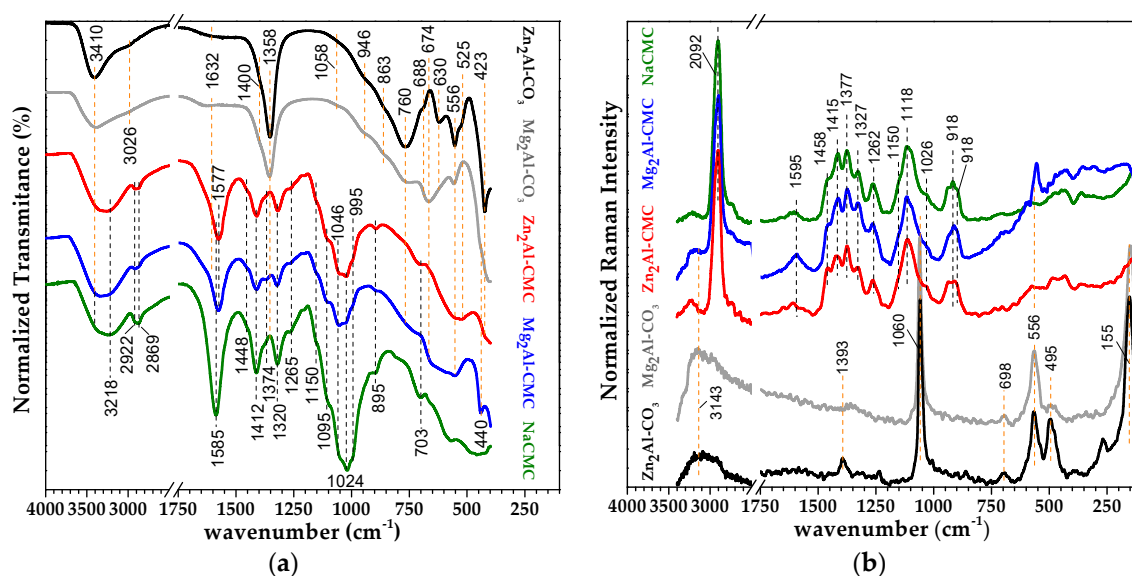


**Figure 4.** FTIR-ATR (a) and FT-Raman (b);  $\lambda_{exc} = 1064$  nm) spectra of  $Zn_2Al-CO_3$  (black),  $Mg_2Al-CO_3$  (grey),  $Zn_2Al-CMC$  (red),  $Mg_2Al-CMC$  (blue) and sodium carboxymethylcellulose (NaCMC, green).

**Table 1.** Vibrational spectroscopic data of sodium carboxymethylcellulose.

Raman	IR	Tentative of Attribution	Reference
3400–3200	3600–3300 (bb)	$\nu OH$ free or hydrogen bonded	[28–30]
2902	–	$\nu CH$	[28,30]
–	2922	$\nu asC(6)H_2$	[28]
–	2869	$\nu sC(6)H_2$	[28]
1595	1585	$\nu asCOO-$	[31]
1458(sh)	–	$\delta scC(6)H_2$	[30,32]
–	1448(sh)	$\delta scCH_2$ and $\delta ipCOH$	[29,32]
1415	–	$\delta CH_2$ and $\delta CCH$ , $\delta HCO$ , $\delta COH$	[30,32]
–	1412	$\nu sCOO-$	[31]
1377	1374(sh)	$\delta CH_2$ and $\delta CCH$ , $\delta HCO$ , $\delta COH$	[30,32]
1327	1320	$\delta wC(6)H_2$ and $\delta CCH$ , $\delta HCO$ , $\delta COH$	[30,32]
1262	1264	$\delta twC(6)H_2$ and $\delta CCH$ , $\delta HCO$ , $\delta COH$	[30,32]
1150(sh)	1150(sh)	$\nu asC-C$ and $\nu asC-O$ (ring breathing)	[29,32]
1118	–	$\nu sC(1)-O-C(4)$ and $s$ ring breathing	[32]
–	1095(sh)	$\nu C(2)-O$	[29,33]
–	1046(sh)	$\delta C(6)-O$ and $\delta C(5)-O$	[33]
1026(sh)	1019	$\delta C(3)-O$	[33]
–	995 (sh)	$\nu C(1)-O$	[33]
918	–	$\delta C(5)C(6)-H$ and $\delta HC(6)O$	[30]
896	895	$\delta C(1)-H$	[32]
–	703	$\delta rkCH_2$ and $\delta oopCOH$ (C6 and C3)	[29,34]

bb = broad band; sh = shoulder;  $\nu$  = stretching;  $as$  = antisymmetric;  $s$  = symmetric;  $\delta$  = bending;  $w$  = wagging;  $tw$  = twisting;  $sc$  = scissoring;  $ip$  = in-plane;  $oop$  = out-of-plane;  $rk$  = rocking.

Thermal analysis technique indicated significant changes in the CMC thermal profile before and after the intercalation process. In the pristine form and under  $N_2$  atmosphere, NaCMC exhibits four events of mass loss until  $1000$  °C (Figure S2, Supplementary Materials). The first event, endothermic, occurring from room temperature up to about  $170$  °C is attributed to the release of a total of  $7.3$  % of the initial mass as water molecules (release of fragment  $m/z = 18$ ) presented initially in the hydrophilic polymer. According to TGA and DSC data, the polymer decomposition occurs in two exothermic steps [35,36]. The first step, steeper, in the  $240$ – $320$  °C range, promotes release of water ( $m/z = 18$ ),

decarboxylation with  $\text{CO}_2$  ( $m/z = 44$ ) release and a low amount of  $\text{C}_3\text{H}_5$  ( $m/z = 41$ ); the second step, in the 320–530 °C range, yields a charred residue. The last event of mass loss, also endothermic, recorded above 800 °C can be related to the decomposition of carbonaceous matter to  $\text{Na}_2\text{CO}_3$  [35]. CMC used in this study has 0.7 of the degree of substitution (*DS*) of carboxymethyl group and, as a result, the repeating unit (RU) can be represented by  $\text{C}_6\text{H}_{10}\text{O}_5(\text{C}_2\text{H}_2\text{O}_2\text{Na})_{0.7}$ . Considering this composition, the expected percentage of  $\text{Na}_2\text{CO}_3$  residue (13.7%) is very close to the experimental value (13.5%) obtained by TGA analysis (Figure S2).

The knowledge of the thermal behavior of carbonate LDH phases and the products produced in distinct temperatures is important to contrast with thermal properties of LDH-CMC precursors. According to TGA-MS results, for both carbonate-based layered structures, three main events of mass loss can be described (Figure 5). The first event, ranging from room temperature up to 220 °C is related to the release of interlayer and adsorbed water molecules [37], as indicated for MS curve (release of  $m/z = 18$  fragment). The initial structure is proven to be modified even at temperatures above 100 °C owing to the detection of growing quantities of  $m/z = 44$  ( $\text{CO}_2$ ) fragment in MS analysis. In the second event of mass loss at temperatures above 200 °C, composition integrity of the layered structure is severely affected owing to the release of water molecules ( $m/z = 18$ ) through a mechanism known as dehydroxylation [37]. For  $\text{Zn}_2\text{Al-CO}_3$ , the onset DSC temperature for dehydroxylation was observed at a lower temperature (215 °C) in comparison to  $\text{Mg}_2\text{Al-CO}_3$  (282 °C), and thus it can be inferred that the  $\text{Mg}_2\text{Al-CO}_3$  structure is thermally more stable than the analogous phase of zinc.

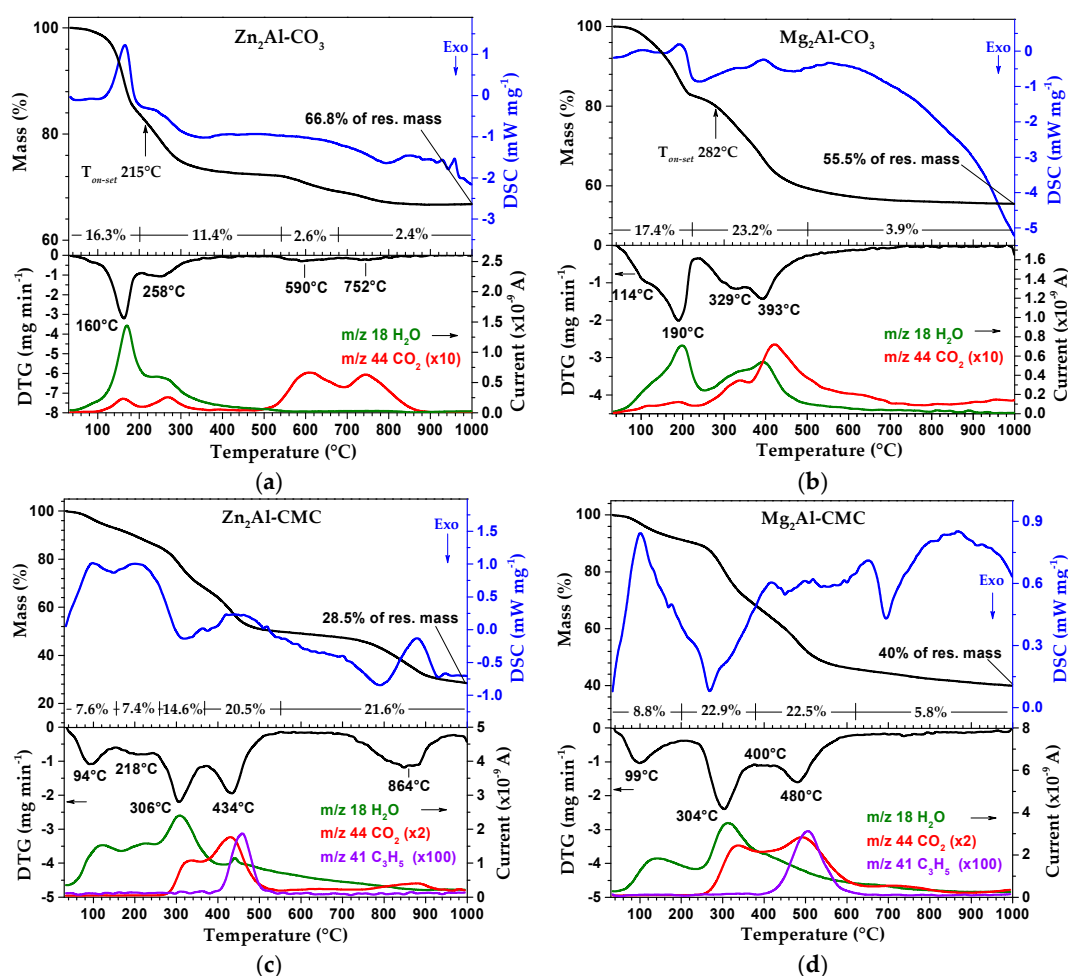


**Figure 5.** TG-DSC and DTG-MS curves of  $\text{Zn}_2\text{Al-CO}_3$  (a),  $\text{Mg}_2\text{Al-CO}_3$  (b),  $\text{Zn}_2\text{Al-CMC}$  (c) and  $\text{Mg}_2\text{Al-CMC}$  (d) samples under  $\text{N}_2$  atmosphere.

Around the same temperature value and at higher temperatures, the release of  $m/z = 44$  fragment ( $\text{CO}_2$ ) is intensified for  $\text{Mg}_2\text{Al-CO}_3$  as the third event of mass loss (decarbonation process) occurs. At around  $480\text{ }^\circ\text{C}$ , dehydroxylation is ended for  $\text{Mg}_2\text{Al-CO}_3$  sample but carbonate decomposition (release of  $m/z = 44$  fragment) is still observed at temperatures up to  $700\text{ }^\circ\text{C}$  (even though the majority of carbonate decomposes at around  $440\text{ }^\circ\text{C}$ ). On the other hand,  $\text{Zn}_2\text{Al-CO}_3$  material exhibits a distinct thermal behavior. Even though it dehydroxylates and is partially decarbonated (since the  $m/z = 44$  fragment analysis reveals the increase of  $\text{CO}_2$  detection above  $200\text{ }^\circ\text{C}$ ), only a small fraction of carbonate ions is released. Just at temperature values higher than  $520\text{ }^\circ\text{C}$ ,  $m/z = 44$  fragment is detected in large quantities in an apparent two distinct mechanisms of mass loss up to  $840\text{ }^\circ\text{C}$ . Such differences in the decarbonation process for  $\text{Zn}_2\text{Al-CO}_3$  compared to  $\text{Mg}_2\text{Al-CO}_3$  can be a direct consequence of the occurrence of dehydroxylation of the Zn-based LDH at lower temperatures than the thermal decomposition of carbonate, which allows the coordination of  $\text{CO}_3^{2-}$  ion to metals present in the formed mixed oxide structure, increasing the anion thermal stability [22,23]. As the temperature of the analysis is increased, after dehydroxylation of the LDH is completed, it is formed an amorphous  $\text{M}^{2+}(\text{Al})\text{O}$  oxide phase, followed by the formation of crystalline oxide phases. Above temperature values of  $500$  and  $800\text{ }^\circ\text{C}$ , spinel phases are obtained respectively for  $\text{Zn}_2\text{Al-CO}_3$  and  $\text{Mg}_2\text{Al-CO}_3$  [23,38,39].

For  $\text{Zn}_2\text{Al-CMC}$ , the dehydration step occurs within the  $30\text{--}250\text{ }^\circ\text{C}$  temperature range, closely followed by  $\text{Mg}_2\text{Al-CMC}$  in the  $30\text{--}225\text{ }^\circ\text{C}$  range according to the increase in the amount of the  $m/z = 18$  ( $\text{H}_2\text{O}$ ) fragment detected (Figure 5). The second event of mass loss (from  $250$  to  $380\text{ }^\circ\text{C}$ ) is related to the thermal decomposition of polymer chains through release of water molecules ( $m/z = 18$ ) from hydroxyl groups in the polymer composition and decarboxylation of side groups ( $m/z = 44$ ) for both layered systems, according to DTG data. Although the beginning of this decomposition event is not significantly shifted towards higher temperatures, when pristine NaCMC is compared to the intercalated polymer into LDH galleries, it is noticed that the polymer decomposition event exhibits larger thermal range after immobilization. Hence, the interaction between both inorganic and organic phases delays the start of polymer fragmentation.

Above  $380\text{ }^\circ\text{C}$ , MS curves of  $\text{M}_2\text{Al-CMC}$  phases are altered substantially depending on the composition of the inorganic layers (Figure 5). At higher temperature values, glucose chains undergo fragmentation in both LDH samples yielding not only water and carbon dioxide molecules but also  $\text{C}_3\text{H}_5$  fragments ( $m/z = 41$ ). Even though the beginning of this event is around the same value for both Mg and Zn-based LDH, it is observed that this second decomposition step is extended to a wider temperature range for  $\text{Mg}_2\text{Al-CMC}$  ( $380\text{--}605\text{ }^\circ\text{C}$ ) than for  $\text{Zn}_2\text{Al-CMC}$  ( $380\text{--}520\text{ }^\circ\text{C}$ ). Mass changes are negligible above  $605\text{ }^\circ\text{C}$  for Mg-based hybrid material (Figure 5). On the other hand, the TGA curve of  $\text{Zn}_2\text{Al-CMC}$  reveals one event of mass loss above  $760\text{ }^\circ\text{C}$  which is not observed in the same experiment conducted at air atmosphere (data not shown). This observation is surprising considering that it is expected the release of less volatile compounds at  $\text{N}_2$  atmosphere than at molecular oxygen environment. The ascription of this event will be clarified ahead in view of XRD and SEM data of pyrolyzed materials.

Based on the dehydration process observed by TGA and data from the chemical elementary analysis, a formula is proposed for LDH- $\text{CO}_3$  and LDH-CMC materials synthesized in this work (Table S3). Experimental  $\text{M}^{2+}/\text{Al}^{3+}$  molar ratio is very close to the nominal value for carbonate or CMC intercalated LDH materials. Precursor hybrid materials present about 20–22% in mass of carbon element.

### 3.2. Characterization of MMO/C Composites

LDH-CMC samples pyrolyzed at  $500$ ,  $600$ ,  $800$  and  $1000\text{ }^\circ\text{C}$  (MMO/C nanocomposites) were evaluated by Raman spectroscopy to assess the type of carbonaceous material obtained (Figure 6). Raman spectra of both LDH-CMC pyrolyzed at  $500\text{ }^\circ\text{C}$  still show fluorescence that suppressed vibrational bands, as observed for NaCMC and LDH-CMC precursors (Figure S3).

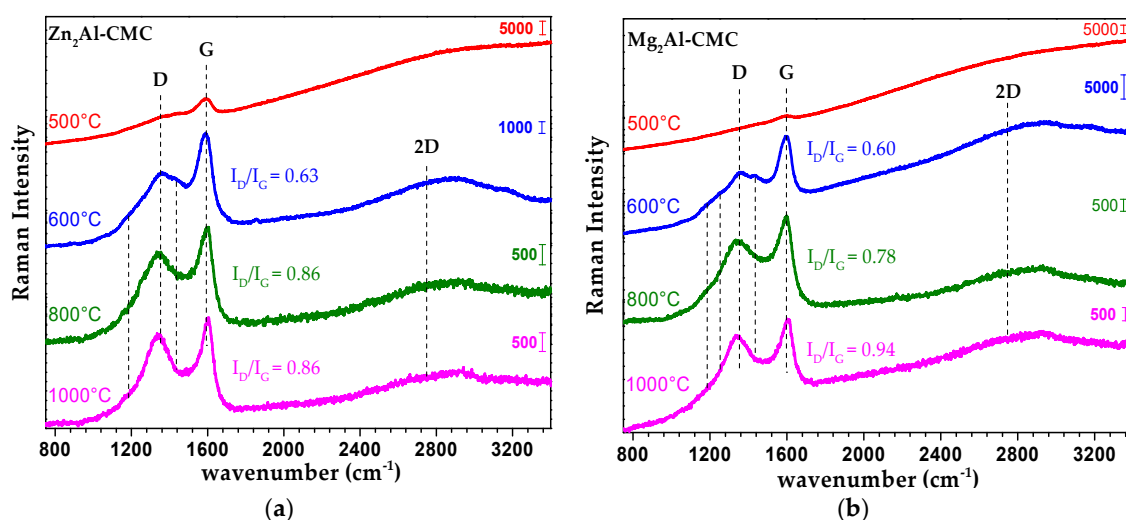


**Figure 6.** Raman spectra of Zn<sub>2</sub>Al-CMC (a) and Mg<sub>2</sub>Al-CMC (b) samples pyrolyzed at 500, 600, 800 and 1000 °C under N<sub>2</sub> atmosphere ( $\lambda_{exc} = 532$  nm).

The characteristic spectral profile of graphitic materials is observed for samples obtained in the 600–1000 °C range (Figure 6): bands D (1340–1350 cm<sup>-1</sup>), G (1590–1600 cm<sup>-1</sup>) and 2D (2500–2800 cm<sup>-1</sup>). Band G is assigned to the in plane stretching of the C=C bonds (Csp<sup>2</sup>) and is characteristic for all forms of sp<sup>2</sup> carbon. Band D is attributed to ring breathing and requires defects for its activation [40–42]. However, besides the graphitic bands, Raman spectra of pyrolyzed samples at 600 °C also exhibit shoulders attributed to amorphous hydrogenated carbonaceous material at 1180 cm<sup>-1</sup> (C–H in aromatic ring structure and correlated to a rich sp<sup>3</sup> structure), 1430 cm<sup>-1</sup> (aromatic ring breathing for rings containing more than two fused aromatic rings), and 1250 cm<sup>-1</sup> (rich sp<sup>3</sup> structure as an aryl-alkyl C–C (like polyacetylene) bonded to aromatic species) [42,43]. These bands disappear with temperature increasing up to 1000 °C. The intensity ratio between bands D and G ( $I_D/I_G$ ) is also increased with temperature progression, pointing out dehydrogenation of carbonaceous material and intensification of aromatic rings [43]. Hence, amorphous carbon is produced between 500 and 600 °C, and yield a more organized structure as the temperature is further increased.

FTIR-ATR spectra of LDH-CMC pyrolyzed materials exhibit weak bands assigned to the organic polymer (Figure 7). A significant change is observed at 1150–990 cm<sup>-1</sup> region, attributed to C–O–C and C–O vibration modes of glycoside rings and to hydroxyl groups, indicating their conversion to other compounds as the temperature is increased. In general, bands observed below 900 cm<sup>-1</sup> are assigned to vibrational modes of M–O bonds as already discussed in Supplementary Materials (Table S2). For comparison purpose, the FTIR-ATR spectra of LDH-CO<sub>3</sub> calcined samples (Figure S4) and the discussion about the results are presented in Supplementary Materials.

To investigate the differences between the thermal transformations of Mg<sub>2</sub>Al-LDH and Zn<sub>2</sub>Al-LDH materials, XRD patterns of samples calcined between 500–1000 °C under N<sub>2</sub> flow were recorded (Figure 8). Zn<sub>2</sub>Al-CMC pyrolyzed and Zn<sub>2</sub>Al-CO<sub>3</sub> calcined at 500 and 600 °C are converted into a poor crystallized ZnO phase. However, at higher temperature values, the products from pyrolysis are very distinctive indicating an influence of the organic polymer in the structure and composition of the inorganic portion of the produced composite. ZnO phase produced from the hybrid LDH at 800 °C is significantly more crystalline than that one obtained from Zn<sub>2</sub>Al-CO<sub>3</sub>. On the other hand, Zn<sub>2</sub>Al-CO<sub>3</sub> is transformed into a well crystallized ZnO and ZnAl<sub>2</sub>O<sub>4</sub> (spinel) phases at 1000 °C, while XRD pattern of Zn<sub>2</sub>Al-CMC presents peaks attributed to ZnAl<sub>2</sub>O<sub>4</sub> and poor crystallized  $\gamma$ -Al<sub>2</sub>O<sub>3</sub> phase. From 800 to 1000 °C, Zn<sub>2</sub>Al-CMC material seems to lose the ZnO phase and this event should be correlated to that one noticed by thermal analysis in the same temperature range (Figure 5).

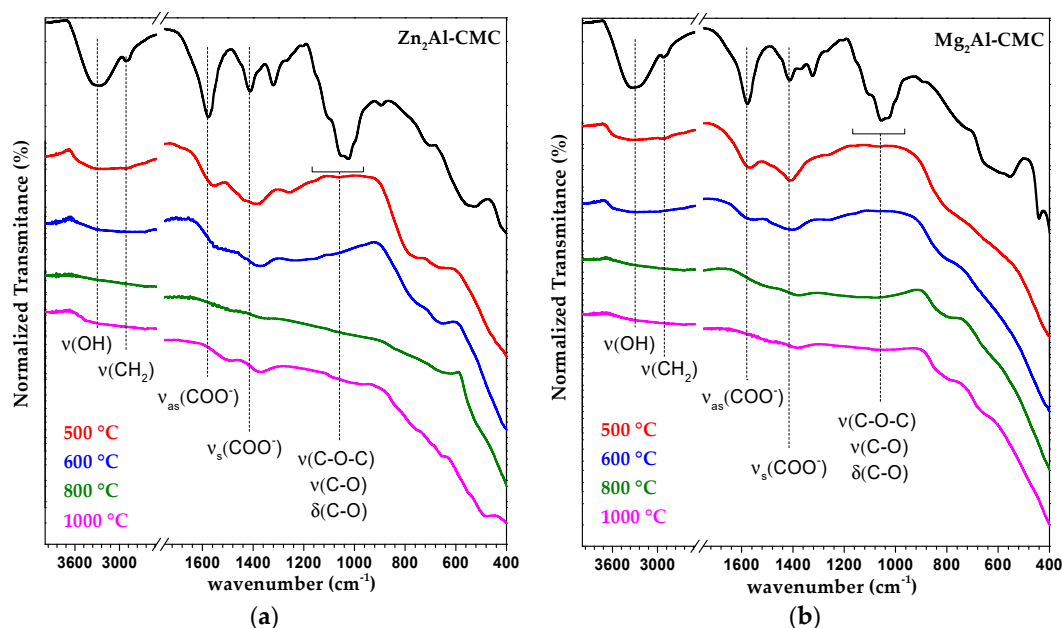


**Figure 7.** FTIR-ATR spectra of Zn<sub>2</sub>Al-CMC (a) and Mg<sub>2</sub>Al-CMC (b) samples pyrolyzed at 500, 600, 800 and 1000 °C under N<sub>2</sub> atmosphere.

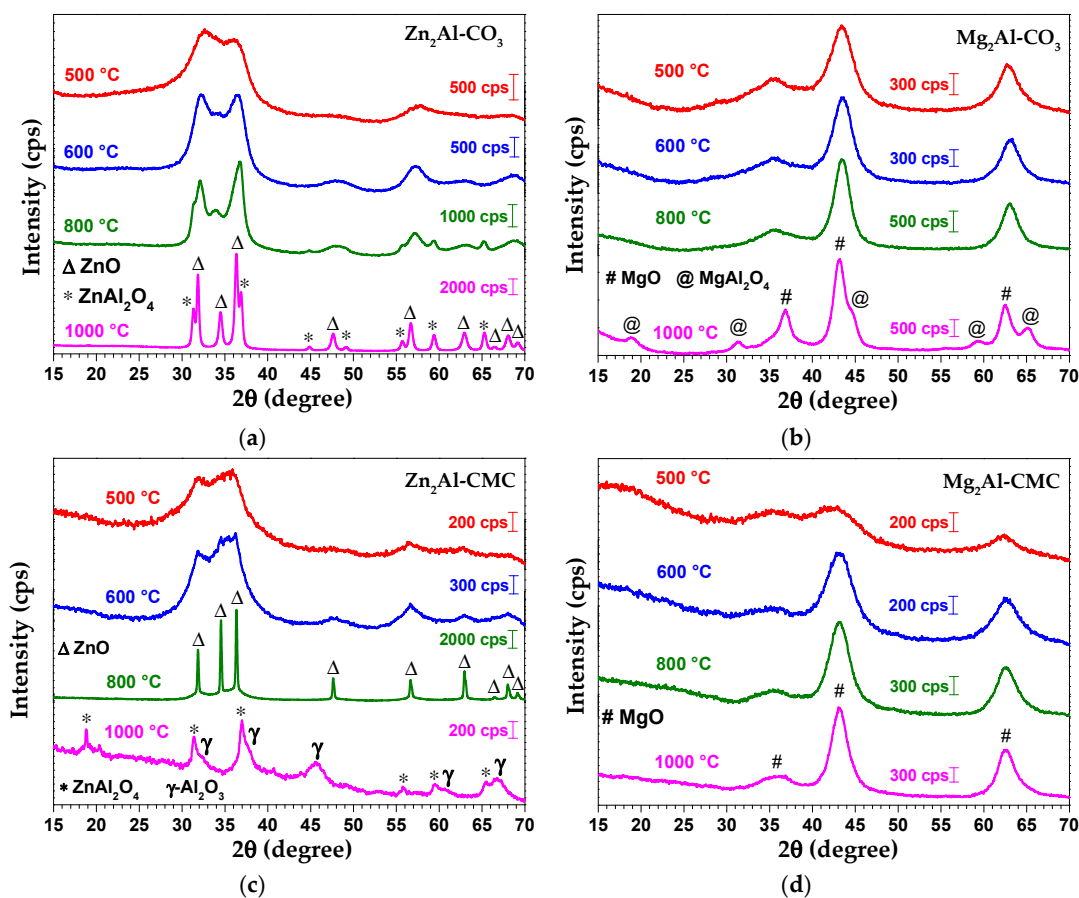


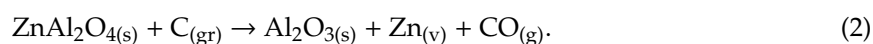
**Figure 8.** XRD patterns of Zn<sub>2</sub>Al-CO<sub>3</sub> (a), Mg<sub>2</sub>Al-CO<sub>3</sub> (b), Zn<sub>2</sub>Al-CMC (c) and Mg<sub>2</sub>Al-CMC (d) samples pyrolyzed at 500, 600, 800 and 1000 °C under N<sub>2</sub> atmosphere. The phases were indicated according to ZnO (wurtzita; ICSD 26170), ZnAl<sub>2</sub>O<sub>4</sub> (ICSD 75091), MgO (periclase; ICSD 9863), MgAl<sub>2</sub>O<sub>4</sub> (ICSD 31373) and γ-Al<sub>2</sub>O<sub>3</sub> (ICSD 249140).

XRD patterns of Mg<sub>2</sub>Al-CMC pyrolyzed between 500–1000 °C indicate the formation MgO phase which crystallinity is increased with the temperature evolution (Figure 8). Similarly, Mg<sub>2</sub>Al-CO<sub>3</sub> sample calcined between 500–800 °C shows reflections of MgO. However, when calcined at 1000 °C, MgO and MgAl<sub>2</sub>O<sub>4</sub> (spinel) phases are observed. The organic polymer intercalated into LDH modified the degree of organization of the inorganic portion of pyrolyzed products. If calcined under an air atmosphere at 1000 °C, both LDH-CMC materials produce metal oxide and spinel phases (Figure S5a) likewise LDH-CO<sub>3</sub> samples under nitrogen atmosphere (Figure 8). In addition, whereas the Mg<sub>2</sub>Al-CMC sample calcined under synthetic air presented less residual mass than that calcined under N<sub>2</sub> at 1000 °C, as it is expected due to carbonized matter, curiously the opposite was observed for Zn<sub>2</sub>Al-CMC sample (Figure S5b).

It can be proposed that graphitic carbonaceous material formed during the pyrolysis of hybrid LDH, and evidenced by Raman spectroscopy (Figure 6), hinders the formation of crystalline spinel phase in the obtained MMO/C nanocomposites, and allows the production of well crystallized ZnO particles at lower temperatures compared to Zn<sub>2</sub>Al-CO<sub>3</sub>. Besides that, comparing the results of thermal analysis (Figure 5), Raman spectroscopy (Figure 6) and XRD (Figure 8), it is proposed that a carbothermic reaction is occurring between 800–1000 °C, i.e., ZnO is reduced to metal form by carbon (from CMC pyrolysis) and released as vapour (zinc boiling point is 920 °C), as represented by the following chemical equation:



Metal zinc is produced by five industrial processes involving mainly the pyrometallurgical method. Carbon is mixed with ZnO and heated at about 1000–1300 °C to produce the metal in the vapour phase [44]. The presence of aluminum oxide at Zn<sub>2</sub>Al-CMC pyrolyzed at 1000 °C can indicate the partial reduction of spinel phase as observed for the mineral gahnite (a zinc aluminate of ZnAl<sub>2</sub>O<sub>4</sub> composition) in the presence of carbon [45]. Hence, a spinel phase decomposition could be represented by the following chemical equation:



A discussion about thermodynamic aspects of reaction (1) can be found in Supplementary Materials (Tables S4 and S5). The carbothermic reaction can explain the disappearance of ZnO diffraction peaks (Figure 8) and the formation of  $\gamma$ -Al<sub>2</sub>O<sub>3</sub> phase. As it is expected, under synthetic air this reaction is not observed because CMC is fully decomposed at 600 °C (data not shown). To the best of our knowledge, this is the first time that carbothermic reaction is reported for zinc-LDH intercalated with organic species.

SEM micrographs shown different morphological transition from LDH to oxides phases according to M<sup>2+</sup> cation composition (M<sup>2+</sup> = Mg<sup>2+</sup> or Zn<sup>2+</sup>). The micrographs of LDH-CMC precursor samples (Figure 9a,b) exhibit a lack of surface distinction among particles, showing up as a continuous mass. This observation can be interpreted as a consequence of small particles formation as already suggested by XRD patterns (Figure 3); morphology of LDH-CMC samples are very distinct of M<sub>2</sub>Al-CO<sub>3</sub> phases, which interparticle frontiers are usually easily distinguished (Figure S6). The presence of the polymer chains also on the external surfaces of LDH particles can contribute to the continuous mass aspect seen in the images. Through an agglomeration process, which occurs along with the sedimentation of particles from reactional media, high surface energies acting over a large number of very small particles can generate such aspect, and behave as a cohesive mass.

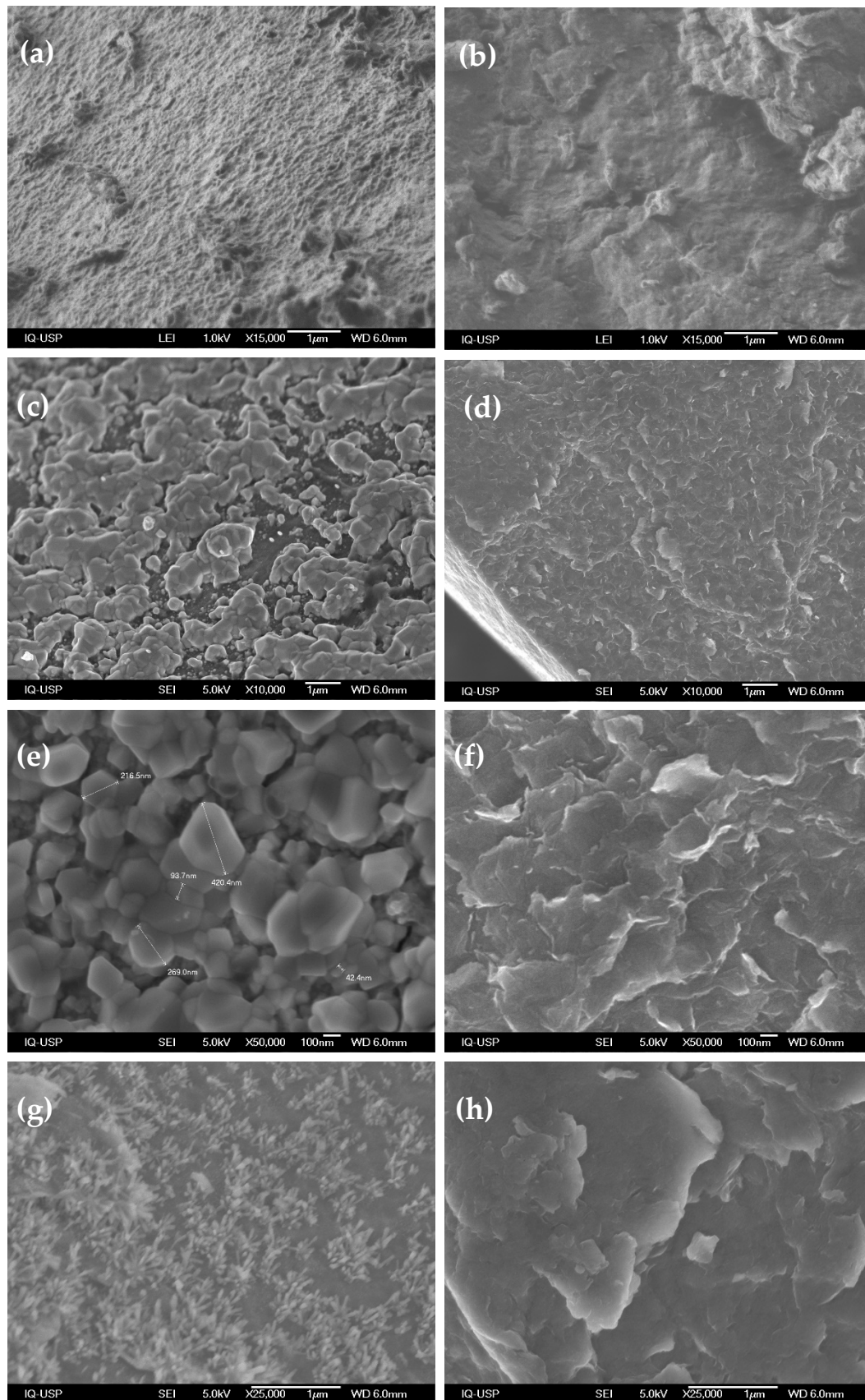


**Figure 9.** SEM micrographs of MMO/C samples obtained from  $Zn_2Al$ -CMC (left) and  $Mg_2Al$ -CMC (right) as synthesized (a,b) and pyrolyzed at 800 (c–f) and 1000 °C (g,h).

Morphological alterations are evident when the pyrolysis process is carried out at 800 °C, producing distinguishable particles at a nanoscale (Figure 9c–f). Thermal decomposition of Zn<sub>2</sub>Al-CMC agglomerates gives rise to denser and zinc/oxygen richer particles as shown respectively by brighter secondary electron contrast (Figure 9c) and EDS spectra (Figure S7). Zn<sub>2</sub>Al-CMC pyrolyzed at 800 °C is composed mainly by well-defined crystallites reaching up to hundreds of nanometers in size and connected through their grain boundaries (Figure 9e). These observations agree with its respective XRD pattern (Figure 6), which evidences the arising of a high crystalline ZnO phase. In comparison, the absence of prominent morphologies is noticed for Mg<sub>2</sub>Al-CMC pyrolyzed at 800 °C (Figure 9d), the sole new feature is the peeling appearance (Figure 9f). Possibly CMC thermal decomposition promotes the weakening and rupture of interfacial interactions among particles, previously acting as an interparticle connector; the subsequent gas evolution from polymer decomposition and matrix dehydroxylation (Figure 5) can also corroborate to the breakdown of the cohesive mass.

A new set of superficial transformations takes place when Zn<sub>2</sub>Al-CMC material is pyrolyzed at 1000 °C (Figure 9g). The zinc rich phase previously observed at 800 °C completely vanishes and a new one emerges, as can be visually depicted mostly as a collection of anisotropic acicular nanocrystals, assembled as branched particles onto the MMO/C composite surface. Besides, EDS spectra collected from this sample reveal considerable decrease in Zn signal (Figure S8). This observation is indicative of ZnO depletion owing to the carbothermic reduction, as suggested by thermal analysis (Figure 5), and XRD pattern recorded for Zn<sub>2</sub>Al-CMC pyrolyzed at 1000 °C (Figure 8). When comparing EDS spectra of acicular particles (Figure S8) to those observed at 800 °C, it is observed an inversion in the intensity between Zn and Al peaks. Branched particles produce EDS spectra with higher aluminum and oxygen intensities compared to those collected from their vicinity, indicating they are composed by Al<sub>2</sub>O<sub>3</sub> (higher Al and O content) as observed by XRD for Zn<sub>2</sub>Al-CMC pyrolyzed at 1000 °C (Figure 8). The superficial features of Mg<sub>2</sub>Al-CMC pyrolyzed at 800 °C are preserved when heated up to 1000 °C (Figure 9h). Also, no significant changes are detected in Mg/Al/O composition by EDS spectroscopy (data not shown) for samples obtained at both high temperature values.

Nanocomposites prepared in this study from a carbon precursor derived from biomass intercalated between LDH based on magnesium and aluminum in the 600–1000 °C range can be explored as adsorbent or catalyst. For example, composite constituted by MgO and biochar obtained by the electrochemical method, which was used for phosphate removal from water [46]. Nanocomposites obtained by Zn<sub>2</sub>Al-CMC pyrolysis in the 600–800 °C range produce incrustated ZnO particles in a matrix of graphitic carbon and spinel phase. Zinc oxide is a semiconductor with potential to be employed in devices for energy production such as dye-sensitized solar cells [47].

#### 4. Conclusions

LDH materials intercalated with CMC polymer, a carbon source derived from biomass, were evaluated as a precursor for the preparation of MMO/C nanocomposites. Best experimental conditions were achieved to get carbon chains between the LDH layers to assure an organic-inorganic interaction at a nanoscale domain. Pyrolysis step conducted above 600 °C produced materials comprising graphitic carbon, which structural organization is increased at higher temperature values. In samples obtained from Mg<sub>2</sub>Al-CMC, the biocarbon presence delays the crystallization of MgO when compared to Mg<sub>2</sub>Al-CO<sub>3</sub> calcined at the same temperature, and also precludes the crystallization of MgAl<sub>2</sub>O<sub>4</sub>. On the other hand, biocarbon formed from Zn<sub>2</sub>Al-CMC pyrolyzed at 800 °C promotes the generation of high crystalline ZnO particles if compared to Zn<sub>2</sub>Al-CO<sub>3</sub> calcined at the same temperature, and also prevents crystallization of ZnAl<sub>2</sub>O<sub>4</sub> phase. Above about 880 °C (endothermic peak in DSC curve), ZnO is reduced by graphitic carbon producing zinc vapour (carbothermic reaction); poor crystallized ZnAl<sub>2</sub>O<sub>4</sub> spinel and  $\gamma$ -Al<sub>2</sub>O<sub>3</sub> phases are noticed after pyrolysis at 1000 °C. Considering the results obtained in this study, to prepare nanocomposites constituted by graphitic carbonaceous material and metal oxides from CMC hybrid materials, the temperature range of pyrolysis process should be 600–800 °C for Zn<sub>2</sub>Al-CMC and 600–1000 °C for Mg<sub>2</sub>Al-CMC. Future studies should investigate

the surface properties of these nanocomposites to explore application in adsorption processes, basic catalysis or photodevices.

**Supplementary Materials:** The following are available online at <http://www.mdpi.com/2305-7084/3/2/55/s1>, Figure S1: XRD pattern of sodium carboxymethylcellulose (NaCMC), Figure S2: TG-DSC and DTG-MS curves of sodium carboxymethylcellulose (NaCMC) under N<sub>2</sub> atmosphere, Figure S3: Raman spectra ( $\lambda_{exc} = 532$  nm) of NaCMC and LDH-CMC samples, Figure S4: FTIR-ATR spectra of Zn<sub>2</sub>Al-CO<sub>3</sub> and Mg<sub>2</sub>Al-CO<sub>3</sub> samples calcined at 500, 600, 800 and 1000 °C under N<sub>2</sub> atmosphere, Figure S5: XRD patterns of M<sub>2</sub>Al-CMC samples calcined at 1000 °C under synthetic air. Pictures of M<sub>2</sub>Al-CMC samples calcined at 1000 °C under synthetic air or nitrogen atmosphere, indicating the percentage of residue after each heating process, Figure S6: SEM image of Mg<sub>2</sub>Al-CO<sub>3</sub> sample, Figure S7: EDS spectra of Zn<sub>2</sub>Al-CMC pyrolyzed at 800 °C, Figure S8: EDS spectra of Zn<sub>2</sub>Al-CMC pyrolyzed at 1000 °C; Table S1: Interplanar distances  $d_{hkl}$  and  $2\theta$  (CuK $\alpha$ ) values from X-ray diffraction data of LDH-CO<sub>3</sub> and LDH-CMC, Table S2: Vibrational data of Zn<sub>2</sub>Al-CO<sub>3</sub> and Mg<sub>2</sub>Al-CO<sub>3</sub>, Table S3: Chemical analysis data and proposed formula for LDH-CO<sub>3</sub> and LDH-CMC, Table S4: Standard molar thermodynamic parameters of substances at 25 °C, Table S5: Standard molar thermodynamic values for the carbothermic reaction between graphitic carbon and zinc or magnesium oxides at 25 °C. Values are calculated using the data presented in Table S4.

**Author Contributions:** Conceptualization, V.R.L.C., G.F.P. and V.R.M.; methodology, V.R.L.C., G.F.P. and V.R.M.; formal analysis, G.F.P., V.R.M. and A.D.; investigation, G.F.P. and V.R.M.; resources, V.R.L.C.; data curation, V.R.L.C.; writing—original draft preparation, V.R.L.C., G.F.P., V.R.M. and A.D.; writing—review and editing, V.R.L.C., G.F.P., V.R.M. and A.D.; visualization, V.R.L.C., G.F.P., V.R.M. and A.D.; supervision, V.R.L.C.; project administration, V.R.L.C.

**Acknowledgments:** This study was financed in part by the Coordenação de Aperfeiçoamento de Pessoal de Nível Superior—Brasil (CAPES)—Finance Code 33002010191P0—Química (scholarship to V.R.M.). V.R.L.C. is thankful to the Conselho Nacional de Desenvolvimento Científico e Tecnológico—Brasil for the research grant (CNPq 305446/2017-7). The authors are also grateful to the Fundação de Amparo à Pesquisa do Estado de São Paulo (FAPESP 2011/50318-1) for financial support and to the Laboratório de Espectroscopia Molecular (LEM-USP) for the Raman and FTIR spectra recording.

**Conflicts of Interest:** The authors declare no conflict of interest.

## References

1. Mills, S.J.; Christy, A.G.; Génin, J.-M.R.; Kameda, T.; Colombo, F. Nomenclature of the hydrotalcite supergroup: Natural layered double hydroxides. *Miner. Mag.* **2012**, *76*, 1289–1336. [[CrossRef](#)]
2. Cavani, F.; Trifirò, F.; Vaccari, A. Hydrotalcite-type anionic clays: Preparation, properties and applications. *Catal. Today* **1991**, *11*, 173–301. [[CrossRef](#)]
3. Evans, D.G.; Slade, R.C.T. Structural Aspects of Layered Double Hydroxides. In *Structure & Bonding*; Springer: Berlin/Heidelberg, Germany, 2006; Volume 119, pp. 1–87. ISBN 3540282793.
4. Taviot-Guého, C.; Prévot, V.; Forano, C.; Renaudin, G.; Mousty, C.; Leroux, F. Tailoring Hybrid Layered Double Hydroxides for the Development of Innovative Applications. *Adv. Funct. Mater.* **2018**, *28*, 1703868. [[CrossRef](#)]
5. Li, T.; Miras, H.; Song, Y.-F. Polyoxometalate (POM)-Layered Double Hydroxides (LDH) Composite Materials: Design and Catalytic Applications. *Catalysts* **2017**, *7*, 260. [[CrossRef](#)]
6. Rives, V.; Angeles Ulibarri, M. Layered double hydroxides (LDH) intercalated with metal coordination compounds and oxometalates. *Coord. Chem. Rev.* **1999**, *181*, 61–120. [[CrossRef](#)]
7. Leroux, F.; Taviot-Guého, C. Fine tuning between organic and inorganic host structure: New trends in layered double hydroxide hybrid assemblies. *J. Mater. Chem.* **2005**, *15*, 3628. [[CrossRef](#)]
8. Rives, V.; del Arco, M.; Martín, C. Intercalation of drugs in layered double hydroxides and their controlled release: A review. *Appl. Clay Sci.* **2014**, *88–89*, 239–269. [[CrossRef](#)]
9. Xu, M.; Wei, M. Layered Double Hydroxide-Based Catalysts: Recent Advances in Preparation, Structure, and Applications. *Adv. Funct. Mater.* **2018**, *28*, 1802943. [[CrossRef](#)]
10. Zubair, M.; Daud, M.; McKay, G.; Shehzad, F.; Al-Harathi, M.A. Recent progress in layered double hydroxides (LDH)-containing hybrids as adsorbents for water remediation. *Appl. Clay Sci.* **2017**, *143*, 279–292. [[CrossRef](#)]
11. Patel, R.; Park, J.T.; Patel, M.; Dash, J.K.; Gowd, E.B.; Karpooomath, R.; Mishra, A.; Kwak, J.; Kim, J.H. Transition-metal-based layered double hydroxides tailored for energy conversion and storage. *J. Mater. Chem. A* **2018**, *6*, 12–29. [[CrossRef](#)]
12. Chimene, D.; Alge, D.L.; Gaharwar, A.K. Two-Dimensional Nanomaterials for Biomedical Applications: Emerging Trends and Future Prospects. *Adv. Mater.* **2015**, *27*, 7261–7284. [[CrossRef](#)] [[PubMed](#)]

13. Erastova, V.; Degiacomi, M.T.G.; Fraser, D.; Greenwell, H.C. Mineral surface chemistry control for origin of prebiotic peptides. *Nat. Commun.* **2017**, *8*, 2033. [[CrossRef](#)] [[PubMed](#)]
14. Debecker, D.P.; Gaigneaux, E.M.; Busca, G. Exploring, tuning, and exploiting the basicity of hydrotalcites for applications in heterogeneous catalysis. *Chem. A Eur. J.* **2009**, *15*, 3920–3935. [[CrossRef](#)] [[PubMed](#)]
15. Yang, Z.; Wang, F.; Zhang, C.; Zeng, G.; Tan, X.; Yu, Z.; Zhong, Y.; Wang, H.; Cui, F. Utilization of LDH-based materials as potential adsorbents and photocatalysts for the decontamination of dyes wastewater: A review. *RSC Adv.* **2016**, *6*, 79415–79436. [[CrossRef](#)]
16. Takehira, K. Recent development of layered double hydroxide-derived catalysts—Rehydration, reconstitution, and supporting, aiming at commercial application. *Appl. Clay Sci.* **2017**, *136*, 112–141. [[CrossRef](#)]
17. Zhao, M.Q.; Zhang, Q.; Huang, J.Q.; Wei, F. Hierarchical nanocomposites derived from nanocarbons and layered double hydroxides—Properties, synthesis, and applications. *Adv. Funct. Mater.* **2012**, *22*, 675–694. [[CrossRef](#)]
18. Kukrety, A.; Singh, R.K.; Singh, P.; Ray, S.S. Comprehension on the Synthesis of Carboxymethylcellulose (CMC) Utilizing Various Cellulose Rich Waste Biomass Resources. *Waste Biomass Valorization* **2018**, *9*, 1587–1595. [[CrossRef](#)]
19. Kang, H.; Huang, G.; Ma, S.; Bai, Y.; Ma, H.; Li, Y.; Yang, X. Coassembly of Inorganic Macromolecule of Exfoliated LDH Nanosheets with Cellulose. *J. Phys. Chem. C* **2009**, *113*, 9157–9163. [[CrossRef](#)]
20. Yadollahi, M.; Namazi, H. Synthesis and characterization of carboxymethyl cellulose/layered double hydroxide nanocomposites. *J. Nanopart. Res.* **2013**, *15*, 1563. [[CrossRef](#)]
21. Yadollahi, M.; Namazi, H.; Aghazadeh, M. Antibacterial carboxymethyl cellulose/Ag nanocomposite hydrogels cross-linked with layered double hydroxides. *Int. J. Biol. Macromol.* **2015**, *79*, 269–277. [[CrossRef](#)]
22. Rocha, M.A.; Petersen, P.A.D.; Teixeira-Neto, E.; Petrilli, H.M.; Leroux, F.; Taviot-Gueho, C.; Constantino, V.R.L. Layered double hydroxide and sulindac coiled and scrolled nanoassemblies for storage and drug release. *RSC Adv.* **2016**, *6*, 16419–16436. [[CrossRef](#)]
23. Zhao, X.; Zhang, F.; Xu, S.; Evans, D.G.; Duan, X. From layered double hydroxides to ZnO-based mixed metal oxides by thermal decomposition: Transformation mechanism and UV-blocking properties of the product. *Chem. Mater.* **2010**, *22*, 3933–3942. [[CrossRef](#)]
24. Hobbs, C.; Jaskaniec, S.; McCarthy, E.K.; Downing, C.; Opelt, K.; Güth, K.; Shmeliov, A.; Mourad, M.C.D.; Mandel, K.; Nicolosi, V. Structural transformation of layered double hydroxides: An in situ TEM analysis. *NPJ 2D Mater. Appl.* **2018**, *2*, 4. [[CrossRef](#)]
25. Miyata, S. Physico-Chemical Properties of Synthetic Hydrotalcites in Relation to Composition. *Clays Clay Miner.* **1980**, *28*, 50–56. [[CrossRef](#)]
26. Elmoubarki, R.; Mahjoubi, F.Z.; Elhalil, A.; Tounsadi, H.; Abdennouri, M.; Sadiq, M.; Qourzal, S.; Zouhri, A.; Barka, N. Ni/Fe and Mg/Fe layered double hydroxides and their calcined derivatives: Preparation, characterization and application on textile dyes removal. *J. Mater. Res. Technol.* **2017**, *6*, 271–283. [[CrossRef](#)]
27. Shang, J.; Shao, Z.; Chen, X. Electrical Behavior of a Natural Polyelectrolyte Hydrogel: Chitosan/Carboxymethylcellulose Hydrogel. *Biomacromolecules* **2008**, *9*, 1208–1213. [[CrossRef](#)]
28. Lee, C.M.; Mohamed, N.M.A.; Watts, H.D.; Kubicki, J.D.; Kim, S.H. Sum-frequency-generation vibration spectroscopy and density functional theory calculations with dispersion corrections (DFT-D2) for cellulose I $\alpha$  and I $\beta$ . *J. Phys. Chem. B* **2013**, *117*, 6681–6692. [[CrossRef](#)]
29. Maréchal, Y.; Chanzy, H. The hydrogen bond network in I( $\beta$ ) cellulose as observed by infrared spectrometry. *J. Mol. Struct.* **2000**, *523*, 183–196. [[CrossRef](#)]
30. Wiley, J.H.; Atalla, R.H. Band assignments in the raman spectra of celluloses. *Carbohydr. Res.* **1987**, *160*, 113–129. [[CrossRef](#)]
31. Cuba-Chiem, L.T.; Huynh, L.; Ralston, J.; Beattie, D.A. Beattie in Situ Particle Film ATR FTIR Spectroscopy of Carboxymethyl Cellulose Adsorption on Talc: Binding Mechanism, pH Effects, and Adsorption Kinetics. *Langmuir* **2008**, *24*, 8036–8044. [[CrossRef](#)]
32. Schenzel, K.; Fischer, S. NIR FT Raman spectroscopy—A rapid analytical tool for detecting the transformation of cellulose polymorphs. *Cellulose* **2001**, *8*, 49–57. [[CrossRef](#)]
33. Barsberg, S. Prediction of vibrational spectra of polysaccharides—simulated IR spectrum of cellulose based on density functional theory (DFT). *J. Phys. Chem. B* **2010**, *114*, 11703–11708. [[CrossRef](#)] [[PubMed](#)]

34. Blackwell, J.; Vasko, P.D.; Koenig, J.L. Infrared and raman spectra of the cellulose from the cell wall of valonia *ventricosa*. *J. Appl. Phys.* **1970**, *41*, 4375–4379. [[CrossRef](#)]
35. Basta, A.H.; El-Saied, H. Characterization of polymer complexes by thermal and ir spectral analyses. *Polym. Plast. Technol. Eng.* **2000**, *39*, 887–904. [[CrossRef](#)]
36. El-Sayed, S.; Mahmoud, K.H.; Fatah, A.A.; Hassen, A. DSC, TGA and dielectric properties of carboxymethyl cellulose/polyvinyl alcohol blends. *Phys. B Condens. Matter* **2011**, *406*, 4068–4076. [[CrossRef](#)]
37. Constantino, V.R.L.; Pinnavaia, T.J. Basic Properties of  $Mg^{2+}_{1-x}Al^{3+}_x$  Layered Double Hydroxides Intercalated by Carbonate, Hydroxide, Chloride, and Sulfate Anions. *Inorg. Chem.* **1995**, *34*, 883–892. [[CrossRef](#)]
38. Belloto, M.; Bernadette, R.; Olivier, C.; John, L.; Dominique, B.; Elkaim, E. A Reexamination of Hydrotalcite Chemistry. *J. Phys. Chem.* **1996**, *100*, 8527–8534. [[CrossRef](#)]
39. Warringham, R.; Mitchell, S.; Murty, R.; Schäublin, R.; Crivelli, P.; Kenvin, J.; Pérez-Ramírez, J. Mapping the Birth and Evolution of Pores upon Thermal Activation of Layered Hydroxides. *Chem. Mater.* **2017**, *29*, 4052–4062. [[CrossRef](#)]
40. Dresselhaus, M.S.; Jorio, A.; Hofmann, M.; Dresselhaus, G.; Saito, R. Perspectives on carbon nanotubes and graphene Raman spectroscopy. *Nano Lett.* **2010**, *10*, 751–758. [[CrossRef](#)] [[PubMed](#)]
41. Ferrari, A.C.; Basko, D.M. Raman spectroscopy as a versatile tool for studying the properties of graphene. *Nat. Nanotechnol.* **2013**, *8*, 235–246. [[CrossRef](#)] [[PubMed](#)]
42. Ferrari, A.C.; Robertson, J. Raman spectroscopy of amorphous, nanostructured, diamond-like carbon, and nanodiamond. *Philos. Trans. R. Soc. Lond. Ser. A Math. Phys. Eng. Sci.* **2004**, *362*, 2477–2512. [[CrossRef](#)] [[PubMed](#)]
43. Kim, P.; Johnson, A.; Edmunds, C.W.; Radosevich, M.; Vogt, F.; Rials, T.G.; Labbé, N. Surface functionality and carbon structures in lignocellulosic-derived biochars produced by fast pyrolysis. *Energy Fuels* **2011**, *25*, 4693–4703. [[CrossRef](#)]
44. Graf, G.G. Zinc. In *Ullmann's Encyclopedia of Industrial Chemistry*; Wiley-VCH Verlag GmbH & Co. KGaA: Weinheim, Germany, 2000; pp. 717–739.
45. Mardones, J.P. Processing of Spinel-Bearing Compounds for Zinc Extraction. Master's Thesis, Delft University of Technology, Faculty of Civil Engineering and Geosciences, Delft, The Netherlands, 2012.
46. Jung, K.-W.; Ahn, K.-H. Fabrication of porosity-enhanced MgO/biochar for removal of phosphate from aqueous solution: Application of a novel combined electrochemical modification method. *Bioresour. Technol.* **2016**, *200*, 1029–1032. [[CrossRef](#)] [[PubMed](#)]
47. Vittal, R.; Ho, K.-C. Zinc oxide based dye-sensitized solar cells: A review. *Renew. Sustain. Energy Rev.* **2017**, *70*, 920–935. [[CrossRef](#)]



© 2019 by the authors. Licensee MDPI, Basel, Switzerland. This article is an open access article distributed under the terms and conditions of the Creative Commons Attribution (CC BY) license (<http://creativecommons.org/licenses/by/4.0/>).